CrystEngComm

Accepted Manuscript

CrystEngComm

ARTICLE

Combinatorial approach to solution-processed $InGaO_3(ZnO)_m$ superlattice films: Growth mechanisms and their thermoelectric properties

Received 00th January 20xx,
Accepted 00th January 20xx

DOI: 10.1039/x0xx00000x

www.rsc.org/

Sung Woon Cho[a], Myoungho Jeong[b,c], Jun Hyeon Kim[a], Yong Hun Kwon[a], Hyoungsub Kim[a], Jeong Yong Lee[b,c] and Hyung Koun Cho[a,*]

Multicomponent amorphous InGaZnO thin films with several metal cations have been synthesized with flexible chemical composition control based on a sol-gel process, and a combinatorial approach through sol-gel process enable us to perform systematic survey to fluently find the best film properties. Contrary to amorphous films, crystalline $InGaO_3(ZnO)_m$ requires refined chemical composition ratio among metal cations. These ratios are expected to affect the growth evolution and thermoelectric properties of two-dimensional $InGaO_3(ZnO)_m$ superlattice structures with various compositional combinations. Here, we explore a combinatorial approach to the ratio of metal cations using various mole fractions of metal precursors in InGaZnO sol for amorphous InGaZnO films fabricated on epitaxial ZnO buffer layer, and then they were crystallized with various chemical compositions. The crystallized $InGaO_3(ZnO)_m$ films can be classified as strong single-phase $InGaO_3(ZnO)_m$, double-phase $InGaO_3(ZnO)_m$/ $InGaO_3(ZnO)_{m+1}$, and weak single-phase $InGaO_3(ZnO)_m$ with excess metal ions. Among them, the strong single-phase $InGaO_3(ZnO)_m$ films with superlattice structures showed superior thermoelectric power factors. The detailed microstructural growth evolution of single- and double-phase $InGaO_3(ZnO)_m$ films were investigated using transmission electron microscopy.

1. Introduction

Hosono et al. proposed a novel oxide semiconductor composed of single crystalline $InGaO_3(ZnO)_m$ with a two-dimensional periodic superlattice structure and have fabricated oxide-based thin film transistors (TFTs) with high mobility (~ 80 cm^2 V^{-1} s^{-1}) due to reduced effective mass of electrons by quantum confinement effect.[1] However, a subsequent and more innovative approach using low process temperature was suggested by the same group for amorphous In-Ga-Zn-O (InGaZnO) alloying compounds, which have been actively employed as channel layers for flat panel displays, as an alternative to existing Si-based TFTs such as amorphous Si and low-temperature polycrystalline Si.[2] Thus, significant attention has been paid to the development of amorphous oxide semiconductors, and technical interest in the single crystalline $InGaO_3(ZnO)_m$ films almost disappeared due to the high temperature process (~ 1400 °C) and unconfirmed application field.

Until recently, semiconducting or semi-insulating superlattice films were widely accepted as novel active structures due to the observation of quantum confinement effects and excellent physical properties.[3-5] Firstly, an example of specifying a superlattice structure is the III-V compounds semiconductors such as InGaAlP, InGaN, and AlGaAsP alloys.[6,7] These superlattice-based III-V thin films have been utilized as active layers in applications such as giant magnetoresistance, laser diodes, and light-emitting diodes.[8-10] Next, several groups reported dramatically enhanced thermoelectric performance by introducing various superlattices in traditional thermoelectric complex materials such as Bi_2Te_3/Bi_2Se_3 and PbTe/PbSe.[11,12] Their thermoelectric properties were effectively modified by controlling the thickness of each layer in superlattice structure.[13,14] Anisotropic superlattice structures can improve thermoelectric figure of merit (ZT) values by taking advantage of the sharp electron density of states function due to quantum confinement effect for Seebeck coefficient, and frequent interface scattering of the phonons for thermal transport.[15-19] Furthermore, oxide materials based on superlattice structures such as Bi_2O_2/Cu_2Se_2 and $SrTi_{1-x}Nb_xO_3/SrTiO_3$ have also exhibited enhanced Seebeck coefficient and ZT values compared with their bulk materials.[20,21]

[a] School of Advanced Materials Science and Engineering, Sungkyunkwan University, 2066 Seobu-ro, Jangan-gu, Suwon, Gyeonggi-do, 16419, Republic of Korea
E-mail : chohk@skku.edu; Tel.: +82 31 299 4733; fax: +82 31 290 7410;
[b] Center for Nanomaterials and Chemical Reactions, Institute for Basic Science (IBS), 291 Daehak-ro, Yuseong-gu, Daejeon, 305-701, Republic of Korea
[c] Department of Materials Science and Engineering, Korea Advanced Institute of Science and Technology (KAIST), 291 Daehak-ro, Yuseong-gu, Daejeon, 305-701, Republic of Korea

† Footnotes relating to the title and/or authors should appear here.
Electronic Supplementary Information (ESI) available: [details of any supplementary information available should be included here]. See DOI: 10.1039/x0xx00000x

Generally, the homogenous crystallization of $InGaO_3(ZnO)_m$ film with a natural superlattice structure, where InO_2^- and $GaO^+(ZnO)_m$ layers are alternatively stacked along the c-axis, has required high temperature to guarantee poly (> 700 °C)[22] and single (> 1400 °C)[23] crystal phases. In contrast, we have already reported the formation of single crystalline $InGaO_3(ZnO)_m$ films heterogeneously crystallized using ZnO buffer layers at reduced temperatures (900 °C).[24,25] These buffer layers are helpful for reducing the critical energy required for the crystallization of $InGaO_3(ZnO)_m$ films by considerably decreasing the lattice mismatch between the $InGaO_3(ZnO)_m$ and substrate. In our first approach, we used epitaxial ZnO films and a sputtered InGaZnO target, and the resulting sample was thermally annealed for crystallization at 900 °C, resulting in the formation of single crystalline $InGaO_3(ZnO)_m$.[24] Next, we have used amorphous InGaZnO (a-InGaZnO) films prepared via wet-based spin coating instead of sputtering InGaZnO films[25]. Furthermore, it is identified that single crystalline $InGaO_3(ZnO)_2$ film with specific m value (m = 2) and superlattice structure shows two-fold increased Seebeck coefficient and dramatically low thermal conductivity (1.11 W m^{-1} K^{-1}) compared to those of ZnO[26,27] and In_2O_3[28] with three-dimensional structure. Contrary to amorphous films, crystalline $InGaO_3(ZnO)_m$ requires ideal stoichiometric composition ratio among metal cations. While the thickness of the InO_2^- layer in crystalline $InGaO_3(ZnO)_m$ remains unchanged, the thickness of the $GaO^+(ZnO)_m$ layer is varied through the selection of m.[29-31] The m value of $GaO^+(ZnO)_m$ layer is naturally determined by the compositional ratio of metal ions in $InGaO_3(ZnO)_m$ superlattice. Thus, we believe that the microstructural and thermoelectric properties of the $InGaO_3(ZnO)_m$ superlattice can dramatically be influenced by the compositional ratio of metal ions, as complex or other oxide thermoelectric materials with superlattice structure. However, combinatorial approach about various compositional ratios of metal ions in $InGaO_3(ZnO)_m$ superlattice films have not been performed due to the difficulties of composition control on previous vacuum-based and high temperature process.

In this study, we prepared various a-InGaZnO films with various metal cation ratios on the ZnO buffer layers through combinatorial approach using sol-gel process which easily and fluently can control chemical composition, like the solution-processed a-InGaZnO channels in the oxide TFTs. Following thermal treatment, we obtained crystallized $InGaO_3(ZnO)_m$ films with superlattice structures, and compared the compositional and microstructural changes via thermal annealing of these films. The basic thermoelectric properties (Seebeck coefficient, electrical resistivity, and power factors) of these $InGaO_3(ZnO)_m$ products were analyzed. Furthermore, we investigated detailed microstructural evolution during the thermal annealing process and the formation of superlattice structures using transmission electron microscopy (TEM).

2. Experimental

The entire sub-sequential process to prepare crystalline $InGaO_3(ZnO)_m$ films with various chemical compositions was designed with three steps: i) an epitaxial ZnO buffer layer (sputtering), ii) the a-InGaZnO layer (sol-gel), and iii) the

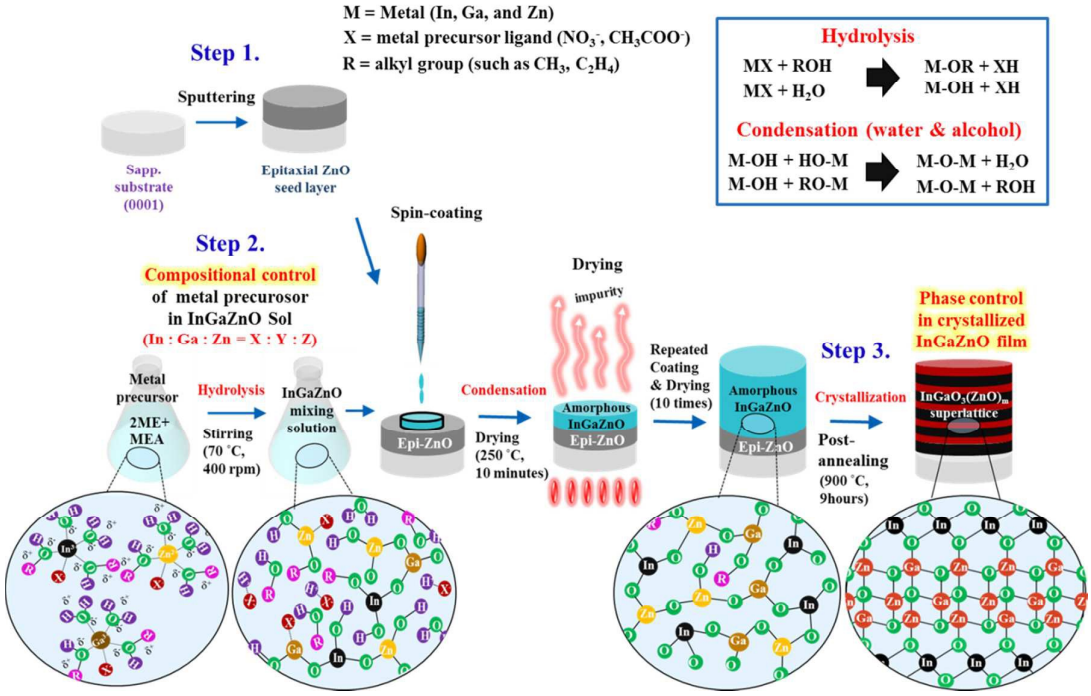

Fig. 1. Overall schematic illustration on the growth process (Steps 1, 2, and 3) and compositional control of solution-processed $InGaO_3(ZnO)_m$ superlattice films through the combinatorial approach: Step 1. Epitaxial ZnO buffer layer deposition (sputtering), Step 2. a-InGaZnO layer deposition (sol-gel), and Step 3. formation of crystallized $InGaO_3(ZnO)_m$ superlattice films (high-temperature annealing).

formation of the $InGaO_3(ZnO)_m$ superlattice (high temperature annealing), as shown in Fig. 1.

Step 1 : Epitaxial ZnO buffer layer deposition (sputtering)

The c-plane sapphire substrates were cleaned via sequential sonication for 10 min each in acetone, ethanol, and deionized water, and then dried in an oven at 70 °C for 1 hour. The ZnO buffer layers were epitaxially prepared on sapphire substrates via radio frequency magnetron sputtering to suppress lattice mismatch between the sapphire substrate and $InGaO_3(ZnO)_m$ crystals, as well as to provide seed sites for solid phase epitaxy at relatively reduced temperatures. The ZnO buffer layers were deposited at 700 °C and under a mixed gas atmosphere (15 mTorr) of Ar/O_2 (20/10 sccm). The thickness of the ZnO was fixed at 50 nm, since it was expected to affect the crystal phase and composition of the crystallized $InGaO_3(ZnO)_m$ films[24].

Step 2 : a-InGaZnO layer deposition (sol-gel)

Preferentially, metal precursors of various combinatorial ratios (In : Ga : Zn = X : Y : Z) among In, Ga, and Zn cations were dissolved in 2-methoxyethanol (2-ME, $C_3H_8O_2$) solvent of 10 mL to 0.2 M total metal concentration in a glove box under a nitrogen atmosphere and low moisture. Indium nitrate hydrate [$In(NO_3)_3{\cdot}xH_2O$, Aldrich], gallium nitrate hydrate [$Ga(NO_3)_3{\cdot}xH_2O$, Aldrich], and zinc acetate dehydrate [$Zn(CH_3COO)_2{\cdot}2H_2O$, Aldrich] were used as metal precursors of In, Ga, and Zn, respectively. 0.3 M monoethanolamin (MEA, C_2H_7NO) was also added as a stabilizer to improve solubility and produce a homogeneous InGaZnO mixing solution. Constant magnetic stirring at 400 rpm on a 70 °C hot plate for 1 hour ensured that each metal precursor (indium nitrate hydrate, gallium nitrate hydrate, and zinc acetate dehydrate) was homogeneously decomposed to M-OH (M = In, Ga and Zn) through hydrolysis, as in the following reactions: $In(NO_3)_3{\cdot}3H_2O \rightarrow In(OH)_3 + 3HNO_3$, $Ga(NO_3)_3{\cdot}3H_2O \rightarrow Ga(OH)_3 + 3HNO_3$, and $2Zn(CH_3COO)_2{\cdot}2H_2O \rightarrow 2Zn(OH)_2 + 4CH_3COOH$. Homogeneous solutions were aged for 24 hours to yield a stable InGaZnO sol, which was spin coated onto 50 nm ZnO buffer layers at 3000 rpm for 30 s and dried for 10 min at 250 °C per one spin-coating. The In-O, Ga-O, and Zn-O were formed via water and alcohol condensation reaction [M-OH to M-O-M (M = In, Ga, and Zn)] at 230-250 °C as in the following reaction : $xIn(OH)_3 + yGa(OH)_3 + zZn(OH)_2 \rightarrow In_xGa_yZn_zO_a + bH_2O$.[32-35] The thickness of a-InGaZnO films (500 nm) was controlled via repeated spin-coatings and drying processes (10 times).

Step 3: Formation of $InGaO_3(ZnO)_m$ superlattice (high-temperature annealing)

The 500 nm a-InGaZnO films with various chemical compositions (In : Ga : Zn = X : Y : Z) on 50 nm epitaxial ZnO buffer layers were crystallized via post-annealing at 900 °C for 9 hours under air ambient in furnace. The 200 nm crystallized $InGaO_3(ZnO)_m$ films with superlattice structure were produced and consisted of single or double phases depending on the mole fraction of the metal cations.

Characterization

The compositional and microstructural characteristics of the crystallized samples were investigated via x-ray diffraction (XRD) (Bruker D8 DISCOVER) with Cu Kα radiation (λ = 1.54 Å) and transmission electron microscopy (TEM) [JEM-2100F (JEOL)] with a LaB_6 electron source operating at 200 kV. Bright field (BF), high-resolution electron microscopy (HREM) images, and selected area diffraction patterns (SADPs) were observed. Cross-sectional TEM specimens were prepared via mechanical polishing and Ar ion milling. Less developed crystalline $InGaO_3(ZnO)_m$ films were coated with carbon to protect their intrinsic microstructure during mechanical polishing and ion milling, since they consist of small-sized crystals and include some voids. To investigate the effect of compositional and microstructural characteristics on the thermoelectric properties of the crystallized samples, electrical resistivity (ρ) was evaluated using a Hall-effect measurement system (Ecopia, HMS-3000) and the Seebeck coefficient (S) is measured at the 325 K with an in-plane configuration. In contrast, the thermal conductivity was evaluated in the out-of plane configuration with a metal strip of 60 μm at 325 K via 3-ω method. Thus, we provided power factor and thermal conductivity separately, due to different carrier flow directions.

3. Results and discussion

3.1 The synthesis of $InGaO_3(ZnO)_m$ superlattice films

In this experiment, we have observed three distinguishable categories for the final crystallized $InGaO_3(ZnO)_m$ products depending on the mole fraction of metal precursors in InGaZnO sol for 500 nm amorphous InGaZnO films fabricated on the 50 nm ZnO buffer layers. Firstly, the a-InGaZnO films synthesized via spin coating with a mole fraction of In:Ga:Zn (1:1:Z, where Z = integer) in sol precursors produced single-phase $InGaO_3(ZnO)_m$ crystals after the buffer-assisted crystallization process at a high temperature of 900 °C in all samples with different Z integers (Z = 0, 1, and 2). In particular, the 50 nm ZnO leads to the contribution of an additional ZnO mole fraction of exactly 1 to the $InGaO_3(ZnO)_m$ films. Consequently, as shown in Fig. 2a-c, the mole fractions of 1:1:0, 1:1:1, and 1:1:2 (In:Ga:Zn) in metal precursors result in single-phase $InGaO_3(ZnO)_m$ films with m values of 1, 2, and 3, respectively, which indicates the relationship of m = Z + 1 in the 50 nm ZnO buffer and 500 nm a-InGaZnO film before thermal annealing. These final $InGaO_3(ZnO)_m$ films show the absence of ZnO-related peaks at 900 °C annealing, indicating complete intermixing between the ZnO buffer and a-InGaZnO. Also, these crystallized samples exhibit very clear and intense periodic satellite peaks originating from atomically well-aligned arrangement along the c-axis, which was introduced in a previous study.[24] The positions of satellite peaks are exactly matched with theoretically-expected crystal planes corresponding to the (000l) of the $InGaO_3(ZnO)_m$, based on JCPDS cards (No. 38-1104, 40-0252, and 40-0253). The $InGaO_3(ZnO)_1$ phase shows diffraction peaks at 2θ = 10.2, 20.4, and 30.9˚ corresponding to (0003), (0006), and (0009) planes, respectively. The $InGaO_3(ZnO)_2$ phase exhibits diffraction peaks

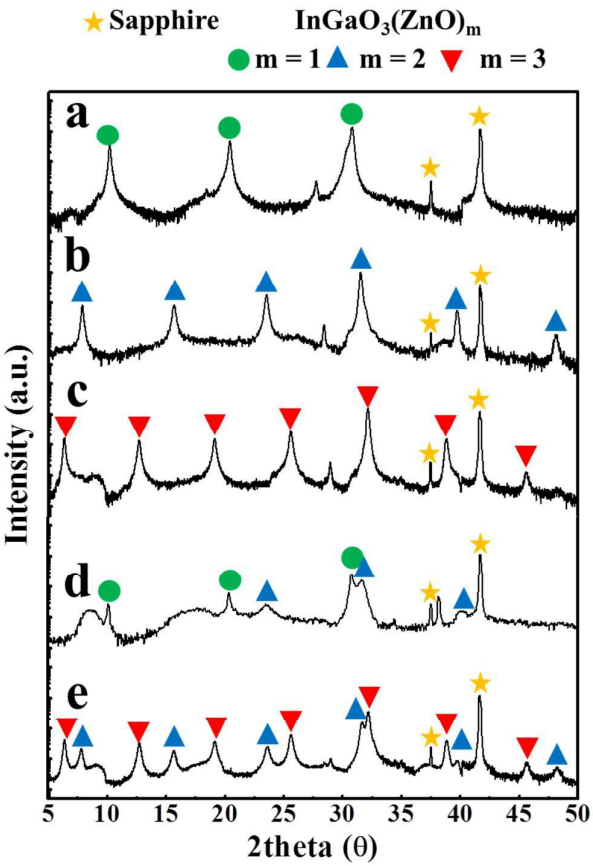

Fig. 2. θ-2θ XRD scans of strong single- (Z = integer) and double- (Z = non-integer) phase $InGaO_3(ZnO)_m$ films using mixing solution with specific mole fractions [In:Ga:Zn = 1:1:Z] among metal precursors ; (a) Z = 0, (b) Z = 1, (c) Z = 2, (d) Z = 0.5, and (e) Z = 1.5.

at 2θ = 7.9, 15.8, 23.8, and 31.9˚, corresponding to the (0002), (0004), (0006), and (0008) planes, respectively. Furthermore, the $InGaO_3(ZnO)_3$ phase discloses diffraction peaks at 2θ = 6.5, 12.9, 19.2, 25.7, and 32.3˚ corresponding to the (0003), (0006), (0009), (00012), and (00015) planes, respectively. For the metal precursor without Zn content (In:Ga:Zn = 1:1:0), the final composition is 1:1:1 and also satisfies the relation of m = Z + 1 in the 50 nm buffer ZnO samples. The low m values of 1, 2, and 3 can be simply produced at relatively low temperature, because high m values have high formation energy and require higher thermal temperature.[23] However, high annealing temperatures lead to the uncontrollable evaporation of metallic In, Ga, and Zn elements, resulting in inhomogeneous final products. Thus, generally low m values are obtained in the crystallized $InGaO_3(ZnO)_m$ films fabricated from ZnO buffer and a-InGaZnO. Thick ZnO buffer layers cause failure in the formation of crystallized $InGaO_3(ZnO)_m$ films due to high m values. As a result, the thickness ratio of 50 nm epitaxial ZnO to 500 nm a-InGaZnO is currently appropriate for the formation of single-phase $InGaO_3(ZnO)_m$ films with superlattice structures. When compared the in-plane lattice parameter $[(a_{InGaO3(ZnO)m}-a_{ZnO}) / a_{ZnO}]$ between $InGaO_3(ZnO)_m$ and ZnO, the high m value of 3 showed reduced lattice mismatch and it is expected that the crystallization process is more active due to low ΔG_{strain}. Nevertheless, all satellite peaks from different $InGaO_3(ZnO)_m$ crystals exhibit similar intensity due to small differences in lattice mismatch: 1.29, 1.19, and 1.07 % in m values of 1, 2, and 3, respectively.

Secondly, we synthesized a-InGaZnO films with the mole fraction In:Ga:Zn (1:1:Z, where Z = non integer) on a ZnO buffer, and produced crystallized $InGaO_3(ZnO)_m$ layers via thermal treatment at 900 °C. These $InGaO_3(ZnO)_m$ films also exhibit crystal diffraction peaks and periodic satellite peaks, as shown in Fig. 2d and e; however, these samples exhibit a blend of two crystal phases, even when given sufficient annealing time. The crystal $InGaO_3(ZnO)_m$ films obtained from Z = 0.5 and 1.5 consisted of two phases corresponding to m = 1 and 2, and m = 2 and 3, respectively, considering the positions of satellite peaks. Also, the intensity of the peaks is relatively weak, but still exhibits distinguishable periodic peaks, indicating that exact control of metal precursors for the formation of single phase $InGaO_3(ZnO)_m$ crystal film is necessary, unlike in a-InGaZnO films.

Next, we synthesized a-InGaZnO films from metal precursors with the mole fraction of In:Ga:Zn = X:Y:1 (X≠Y), where the In/Ga ratio deviated from 1. As shown in Fig. 3, the crystallized $In_xGa_yO_3(ZnO)_m$ films produced from these 500 nm a-InGaZnO films and 50 nm ZnO buffer also feature superlattice structures with periodic satellite peaks, though their diffraction peaks have relatively broad and asymmetric shoulders and low intensity, indicating a less developed superlattice structure in the $In_xGa_yO_3(ZnO)m$ films. The a-InGaZnO films fabricated using a solution process can have various composition ratios due to their amorphous bonding structure with short range

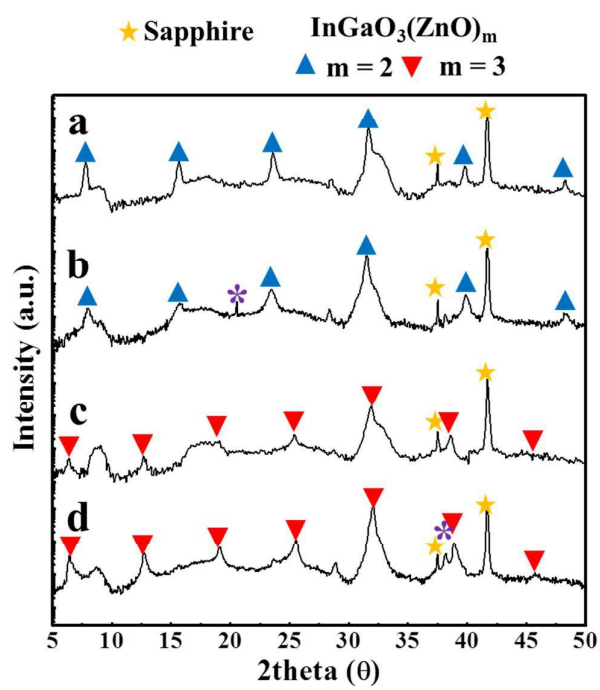

Fig. 3. θ-2θ XRD scans of weak single-phase $InGaO_3(ZnO)_m$ films using a mixing solution with specific mole fractions [In : Ga : Zn = X : Y : 1, X≠Y] among metal precursors ; (a) X : Y = 1 : 1.5, (b) X : Y = 1.5 : 1, (c) X : Y = 1 : 0.5, and (d) X : Y = 0.5 : 1.

Table 1. A summary of the phase formation and compositional contents [In:Ga:Zn] of 200nm $InGaO_3(ZnO)_m$ superlattice films produced via 500 nm a-InGaZnO synthesized using InGaZnO sol with various mole fractions of metal precursors and a 50 nm ZnO buffer.

Metal cation ratio in InGaZnO sol & a-InGaZnO [In : Ga : Zn]		Crystalline $InGaO_3(ZnO)_m$ (Crystallized a-InGaZnO with epi-ZnO : a-InGaZnO + epi-ZnO)				
		Total metal cation ratio [In : Ga : Zn] & phase category		Partial metal cation ratio [In : Ga : Zn] & actual phase		Phase fraction
1 : 1 : Z (Z = interger)	1 : 1 : 0	1 : 1 : 1	Strong single-phase $InGaO_3(ZnO)_m$	1 : 1 : 1	$InGaO_3(ZnO)_1$	1
	1 : 1 : 1	1 : 1 : 2		1 : 1 : 2	$InGaO_3(ZnO)_2$	1
	1 : 1 : 2	1 : 1 : 3		1 : 1 : 3	$InGaO_3(ZnO)_3$	1
1 : 1 : Z (Z = Non -interger)	1 : 1 : 0.5	1 : 1 : 1.5	Double-phase $InGaO_3(ZnO)_m$	0.5 : 0.5 : 0.5	$InGaO_3(ZnO)_1$	0.5
				0.5 : 0.5 : 1	$InGaO_3(ZnO)_2$	0.5
	1 : 1 : 1.5	1 : 1 : 2.5		0.5 : 0.5 : 1	$InGaO_3(ZnO)_2$	0.5
				0.5 : 0.5 : 1.5	$InGaO_3(ZnO)_3$	0.5
X : Y : 1 (X ≠ Y)	1 : 0.5 : 1	1 : 0.5 : 2	Weak single-phase $InGaO_3(ZnO)_m$	0.5 : 0.5 : 1.5	$InGaO_3(ZnO)_3$	0.5
				0.5 : 0 : 0.5	In^{3+} and Zn^{2+}	0.5
	0.5 : 1 : 1	0.5 : 1 : 2		0.5 : 0.5 : 1.5	$InGaO_3(ZnO)_3$	0.5
				0 : 0.5 : 0.5	Ga^{3+} and Zn^{2+}	0.5
	1 : 1.5 : 1	1 : 1.5 : 2		1 : 1 : 2	$InGaO_3(ZnO)_2$	0.666
				0 : 0.5 : 0	Ga^{3+}	0.333
	1.5 : 1 : 1	1.5 : 1 : 2		1 : 1 : 2	$InGaO_3(ZnO)_2$	0.666
				0.5 : 0 : 0	In^{3+}	0.333

order, and their compositions are strongly dependent on only the content of the metal precursors. The stable $In_xGa_yO_3(ZnO)_m$ crystal phases are generally reported to exist as solely In:Ga = 1:1, regardless of m values. From the position of the satellite peaks, we found that the $InGaO_3(ZnO)_2$ and $InGaO_3(ZnO)_3$ crystal phases were formed in the In+Ga of 2.5 and 1.5, respectively, with respect to Zn = 1. In addition, excess metal ions deviated from the In:Ga = 1:1 ratio are expected to hinder the formation of perfect superlattice structures. Consequently, to produce $InGaO_3(ZnO)_m$ crystal films with highly-ordered atomic arrangement along the c-axis, a mole fraction of metal solution precursors with a narrow window is a prerequisite, and the 500 nm a-InGaZnO films on the 50 nm ZnO buffer layers should be synthesized with a In:Ga:Zn ratio of 1:1: (integer 0, 1, and 2). Table 1 features a summary of the phase formation of our $InGaO_3(ZnO)_m$ crystal thin films produced by 500 nm a-InGaZnO with various metal mole fractions and a 50 nm ZnO buffer. When ignoring the contribution of structural factors to diffraction intensity in the samples with various m values, we can estimate the fraction of crystal phase from the diffraction peaks with the strongest intensity, as shown in Table 1.

3.2 A phase diagram showing the thermoelectric properties of $InGaO_3(ZnO)_m$ superlattice films

Fig. 4a shows a combinatorial diagram mapped as a ternary phase diagram of In-Ga-Zn metal ions for crystallized $InGaO_3(ZnO)_m$ film, in which 500 nm a-InGaZnO films deposited on 50 nm ZnO buffer were sufficiently post-annealed, and where the strong single-phase, double-phase, and weak single-phase crystals are indicated by "★", "□", and "o", respectively. In Fig. 4b-d, the Seebeck coefficient (S), electrical resistivity (ρ), and power factor (P.F. = S^2/ρ) are designated in the corresponding compositions of In-Ga-Zn metal ions in crystallized $InGaO_3(ZnO)_m$ films. Interestingly, the $InGaO_3(ZnO)_m$ crystal phases located along the normal center line with an In:Ga ratio of 1:1 show enhanced Seebeck coefficients. These films corresponded to the strong single-phase and double-phase $InGaO_3(ZnO)_m$ crystals with c-axis ordered structures and consist of stoichiometric crystal phases without excess metal ions. Furthermore, the electrical resistivity from the strong single-phase $InGaO_3(ZnO)_m$ films showed extremely low values, below 10 mΩ cm, while double-phase and weak single-phase (excess metals) $InGaO_3(ZnO)_m$ films showed > 100 mΩ cm. The strong single-phase $InGaO_3(ZnO)_m$ film is anticipated to have reduced grain boundaries, while the weak single-phase (excess metals) samples are expected to induce frequent interface scattering for electron charge transport from the boundaries between various phases. Also, the excess metal ions in the less crystallized single-phase hinder the charge transport efficiency. Thus, the defect-related charge scattering from phase boundaries and impurities led to suddenly increased electrical resistivity. Finally, the thermoelectric power factor, S^2/ρ, can be obtained from these values, as shown in Fig. 4d. The higher value of S and lower value of ρ in the strong single-phase $InGaO_3(ZnO)_m$ films leads to an enhanced power factor. According to previous surveys, the bulk ZnO and In_2O_3 based

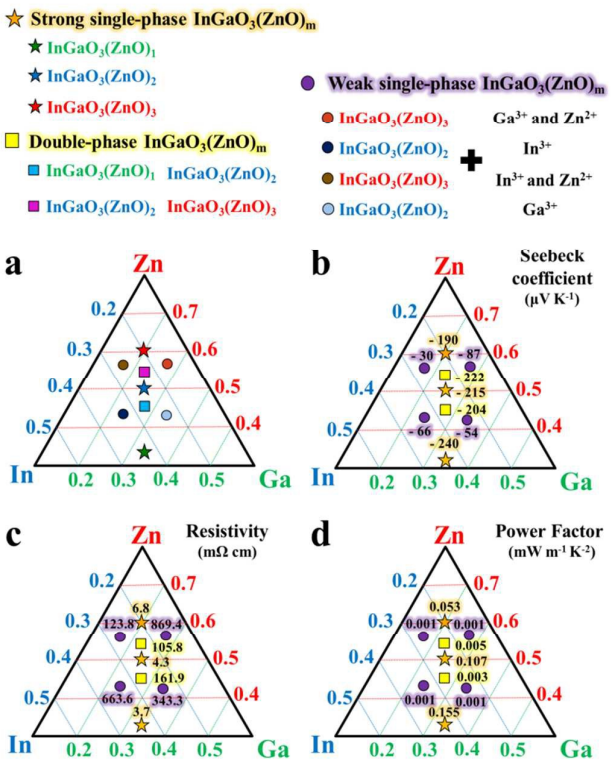

Fig. 4. (a) Combinatorial ternary phase diagram, (b) Seebeck coefficient (S), electrical resistivity (ρ), and power factor (P.F. = S^2/ρ) for corresponding compositions of In-Ga-Zn metal ions in the 200 nm crystallized $InGaO_3(ZnO)_m$ films where 500 nm a-InGaZnO films deposited on 50 nm ZnO buffer were sufficiently post-annealed.

oxides have shown lower Seebeck coefficients (~ -100 μV K^{-1}) and power factor values (~ 10^{-2} mW m^{-1} K^{-2}),[36,37] while well-engineered nano-inclusion, nano-grain, and preferred orientation induced improved Seebeck coefficient (> -200 μV K^{-1}) and power factor (> 10^{-1} mW m^{-1} K^{-2}),[38-40] as our strong single-phase $InGaO_3(ZnO)_m$ films. The thermal conductivity which is another principal factor to evaluate thermoelectric performance was measured from strong single-phase $InGaO_3(ZnO)_m$ superlattice films. Interestingly, their thermal conductivities exhibited low values (0.72 ~ 1.84 W m^{-1} K^{-1} at 325 K) due to dramatically increased phonon scattering from the $InO_2^-/GaO^+(ZnO)_m/InO_2^-$ interfaces, compared to those of typical bulk In_2O_3 and ZnO-based oxides (> 10 W m^{-1} K^{-1}).[36,37] Among those samples, the $InGaO_3(ZnO)_m$ film produced from the 500 nm a-InGaZnO with the reduced Zn fraction and a 50 nm ZnO buffer has a larger power factor than the other samples. The largest power factor was 0.155 mW m^{-1} K^{-2}. These results inform us that the $InGaO_3(ZnO)_m$ films for the thermoelectric application must simultaneously feature a strong single crystallized phase and a well-ordered c-axis structure.

3.3 The microstructural growth evolution of $InGaO_3(ZnO)_m$ superlattice films

Although the XRD patterns provided helpful information on the formation of superlattice structures in the crystallized

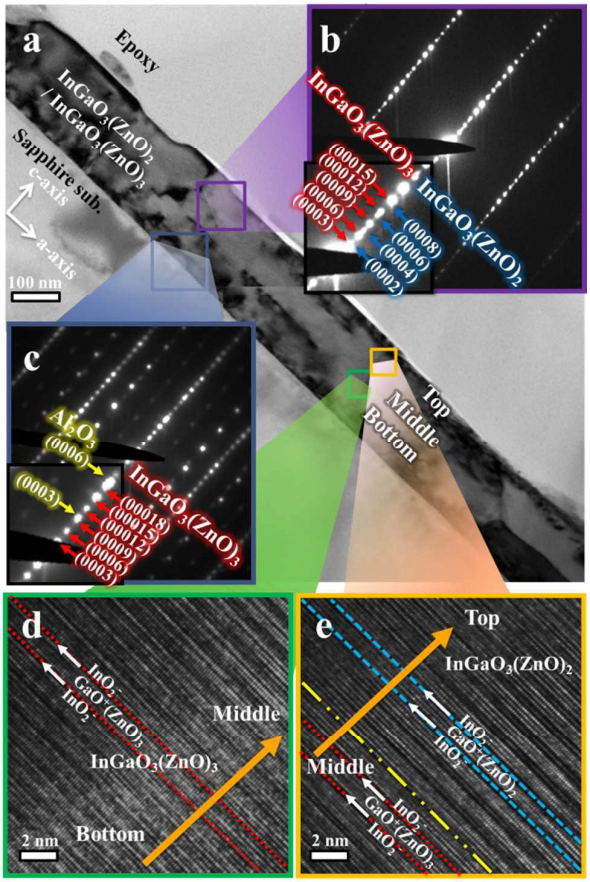

Fig. 5. (a) Bright field image, (b, c) selective area diffraction patterns, and (d, e) HRTEM images of a double-phase $InGaO_3(ZnO)_2/InGaO_3(ZnO)_3$ film showing periodic diffraction spots along the c-axis: (b, e) Top and (c, d) bottom regions.

$InGaO_3(ZnO)_m$ films, we cannot clearly understand the precise microstructural difference and distribution of crystal phases. Thus, we have performed TEM observation of the $InGaO_3(ZnO)_m$ films with double-phase crystals (Fig. 5 and 6) and strong single-phase crystals (Fig. 7). The sample consisting of double-phase crystals was produced by 500 nm a-InGaZnO with an In:Ga:Zn ratio of 1:1:1.5 and 50 nm ZnO, and the final crystal phases consisted of $InGaO_3(ZnO)_2$ and $InGaO_3(ZnO)_3$. The bright-field image using g = 000l shows the absence of vertically-aligned grain boundaries, and it appears as a single crystalline phase like the epitaxial ZnO/sapphire[41] and GaN/sapphire,[42,43] even though the $InGaO_3(ZnO)_m$ film consists of two phases with similar XRD intensities. It is noticeable that the selective area diffraction patterns (SADPs) from the top and bottom regions are not identical, as shown in Fig. 5b and c. Fig. 5c is a traditional SADP from the $InGaO_3(ZnO)_m$ crystals with superlattice structures along the c-axis on a sapphire substrate, and the distance between diffraction peaks indicates that this crystal is $InGaO_3(ZnO)_3$. However, we can detect additional patterns of $InGaO_3(ZnO)_2$ indicated by blue arrows in top region, as shown in Fig. 5b. These spots were also distributed with a periodic distance along the c-axis. We obtained high-resolution TEM images for distinct analysis of microstructural changes (Fig. 5d and e). While the bottom

region shows a homogenous atomic arrangement corresponding to the $InGaO_3(ZnO)_3$ phase, the crystal structure in the middle region of the $InGaO_3(ZnO)_m$ film was transferred from $InGaO_3(ZnO)_3$ to $InGaO_3(ZnO)_2$ with an $InO_2^-/GaO^+(ZnO)_2/InO_2^-$ stacking sequence, as shown in Fig. 5e. These TEM images inform us that the $InGaO_3(ZnO)_m$ in the bottom region features a higher Zn composition of m = 3 and that the top region features a reduced Zn mole fraction of m = 2. This is attributed to the difference in the degree of diffusion from the ZnO buffer layers, considering a determined total Zn mole fraction and a possible crystal structure. Consequently, these results reveal that the double-phase crystal was distributed in vertical stacks like a double layer, and thus there is an absence of vertically-aligned grain boundaries.

We investigated the detailed microstructural evolution of $InGaO_3(ZnO)_m$ with double-phase crystals prepared at various annealing times. Fig. 6 shows XRD patterns, TEM images, and SADPs for the $InGaO_3(ZnO)_m$ films with double-phase crystals annealed for as-dep, 0.5, 3, 6, and 9 hours. In the sample with as-deposited a-InGaZnO/ZnO buffer structure, only the ZnO-related $(0002)_{ZnO}$ peak is observed except the substrate. After thermal annealing for 0.5 h at 900 °C, weak and broad

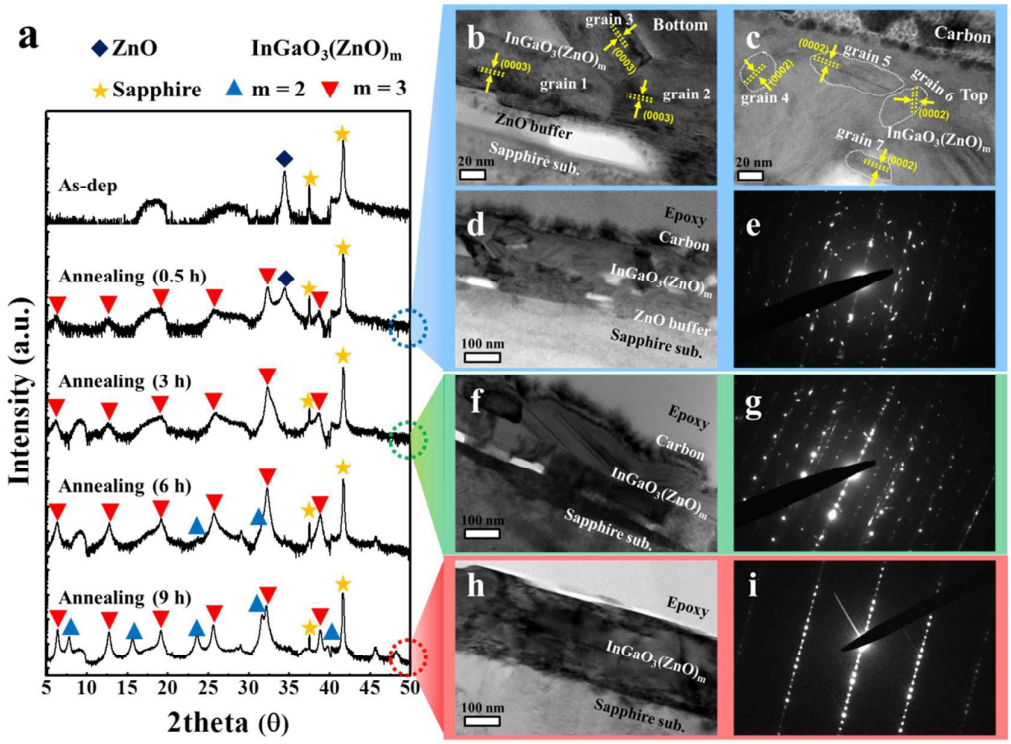

Fig. 6. (a) The growth evolution of double-phase $InGaO_3(ZnO)_2/InGaO_3(ZnO)_3$ superlattice film. θ-2θ XRD scans of double-phase $InGaO_3(ZnO)_2/InGaO_3(ZnO)_3$ based on various post-annealing times: as-dep. (a-InGaZnO), 0.5 h, 3 h, 6 h, and 9 h. Their bright field images and selective area diffraction patterns: (b-e) 0.5 h, (f, g) 3 h, and (h, i) 9 h.

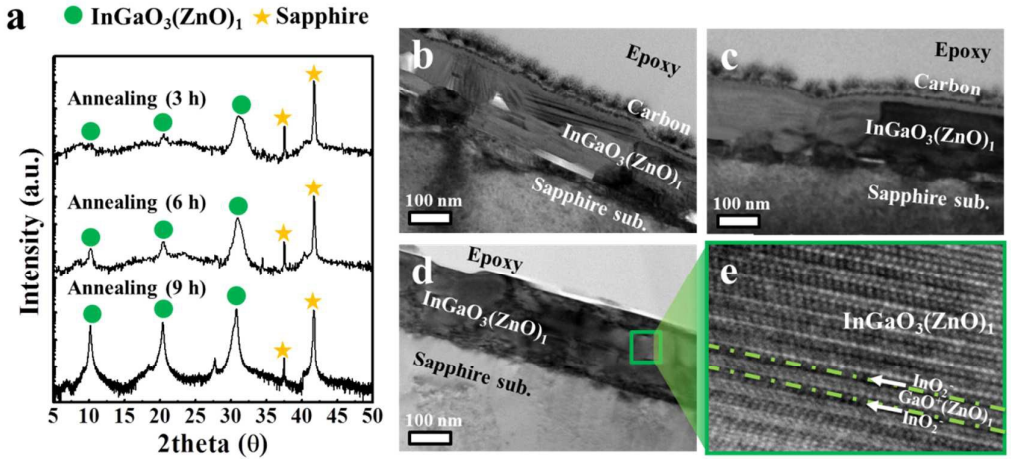

Fig. 7. The growth evolution of strong single-phase $InGaO_3(ZnO)_1$ superlattice film. (a) θ-2θ XRD scans of strong single-phase $InGaO_3(ZnO)_1$ films with various post-annealing times (3, 6, and 9 h). Their bright field images and HRTEM image; (b) 3 h, (c) 6 h, and (d, e) 9 h.

crystallized peaks appear with periodic distances and the $(0002)_{ZnO}$ peak becomes weak. Here, the formed crystals are $InGaO_3(ZnO)_3$ with higher Zn mole fractions, even though the as-deposited samples consisted of 500 nm a-InGaZnO with In:Ga:Zn = 1:1:1.5 and 50 nm ZnO. The well-developed crystal phases are preferentially observed in the bottom region of crystallized $InGaO_3(ZnO)_m$ film near the ZnO buffer (Fig. 6b), and the top region is composed of randomly-arrayed crystal grains with small size; some voids are also observed (Fig. 6c). The sample annealed for 3 hours exhibits a disappearance of the ZnO-related peak, implying complete intermixing between a-InGaZnO and the ZnO buffer. In addition, the diffraction peaks from the crystal phases become strong and the superlattice-like SADPs are also observed (Fig. 6g). However, it is still poly-crystalline $InGaO_3(ZnO)_m$ film including many crystal grains and several voids due to insufficient crystallization. As the annealing time increases, a double-phase crystal appears and the SADPs become distinctly intense. In particular, the final $InGaO_3(ZnO)_m$ crystal film has relatively smooth surface morphology and high density without voids, as well as consists of two crystals of $InGaO_3(ZnO)_2$ and $InGaO_3(ZnO)_3$ (Fig. 6h and i). Here, the line defects located on the (000l) planes are stacking faults produced by thermal annealing and two phase boundaries.

The growth evolution on the $InGaO_3(ZnO)_m$ film with the strong single-phase was also studied. Fig. 7 presents XRD results and TEM images showing microstructural evolution for the 200nm $InGaO_3(ZnO)_1$ film produced from 500 nm a-InGaZnO with In:Ga:Zn = 1:1:0 and 50 nm ZnO buffer. Insufficient annealing time leads to a partially-crystallized film consisting of a complete crystal with high c-axis preferred orientation in the bottom and amorphous or less-developed crystals with random orientation in the top region, as shown in Fig. 7b and c. An enough annealing time of 9 hours produces single-phase $InGaO_3(ZnO)_1$ as the final product, which can be confirmed from XRD patterns, TEM image, and HRTEM image. Fig. 7d and e shows similar TEM images obtained from single crystalline epitaxial ZnO films on the sapphire substrates, though this film still features stacking faults. In addition, its surface morphology is flat as the single crystalline domain, despite going through transition process with rugged morphology in the insufficient annealing. Table 2 shows a summary of thermoelectric properties from these $InGaO_3(ZnO)_1$ films based on annealing time. The sample synthesized under sufficient annealing time exhibits the highest Seebeck coefficient (-240 μV K^{-1}) and lowest electrical resistivity (3.7 mΩ cm), resulting in a high power factor (0.155 mW m^{-1} K^{-2}) due to the suppression of defect generation.

Table 2. A summary of thermoelectric properties [Seebeck coefficient (S), electrical resistivity (ρ), and power factor (P.F.)] from the strong single-phase $InGaO_3(ZnO)_1$ films based on annealing time.

Annealing time	Seebeck coefficient (μV•K^{-1})	Resistivity (mΩ•cm)	Power factor (mW•m^{-1}•K^{-2})
3 hour	-140	8.3	0.023
6 hour	-182	7.0	0.047
9 hour	-240	3.7	0.155

4. Conclusions

We have studied a combinatorial approach to the formation of crystallized $InGaO_3(ZnO)_m$, where a-InGaZnO films (500 nm) with various cation ratios (In:Ga:Zn = X:Y:Z) using a solution-base process (repeatedly spin-coating and drying) were produced on 50 nm epitaxial ZnO buffer layers. The crystallized $InGaO_3(ZnO)_m$ films could be categorized as i) strong single-phase $InGaO_3(ZnO)_m$ from a-InGaZnO of In:Ga:Zn = 1:1:Z (Z = integer), ii) double-phase $InGaO_3(ZnO)_m/InGaO_3(ZnO)_{m+1}$ from In:Ga:Zn = 1:1:Z (Z = non-integer), and iii) weak single-phase $InGaO_3(ZnO)_m$ with excess metal ions from In:Ga:Zn = X:Y:1 (X≠Y). The final $InGaO_3(ZnO)_m$ crystals showed the relationship of m = Z+1 in the 50 nm ZnO buffer and 500 nm a-InGaZnO film due to the interdiffusion caused by high temperature annealing. Resultantly, the double-phase crystallized film was composed of $InGaO_3(ZnO)_{m+1}$ in the bottom region and $InGaO_3(ZnO)_m$ in the top region. The strong single-phase $InGaO_3(ZnO)_m$ superlattice films showed the best thermoelectric power factors due to better Seebeck coefficients and excellent electrical conductivity. In particular, the single-phase $InGaO_3(ZnO)_1$ superlattice films had no grain-boundary, high c-axis preferred orientation, and low stacking fault density, resulting in the most ideal thermoelectric properties (P.F. = 0.155 mW m^{-1} K^{-2}, Seebeck coefficient = -240 μV K^{-1}, electrical resistivity = 3.7 mΩ cm).

Acknowledgements

This work was supported by National Research Foundation of Korea (NRF) grant funded by Basic Research Laboratory project of the Korea government (MSIP) (Grant No. 2014R1A4A1008474) and was also supported by the Human Resources Program in Energy Technology of the Korea Institute of Energy Technology Evaluation and Planning (KETEP) granted financial resource from the Ministry of Trade, Industry & Energy, Republic of Korea (Grant No. 20154030200870).

Notes and references

1 K. Nomura, H. Ohta, K. Ueda, T. Kamiya, M. Hirano and H. Hosono, *Science*, 2003, **300**, 1269-1272.
2 K. Nomura, H. Ohta, A. Takagi, T. Kamiya, M. Hirano and H. Hosono, *Nature*, 2004, **432**, 488-491.
3 L. D. Hicks and M. S. Dresselhaus, *Phys. Rev. B*, 1993, **47**, 727-731.
4 A. Balandin and K. L. Wang, *Phys. Rev. B*, 1998, **58**, 1544-1549.
5 I. Gorczyca and T. Suski, *Cryst. Growth Des.*, 2012, **12**, 3521-3525.
6 W. Lin, S. Li and J. Kang, *Appl. Phys. Lett.*, 2010, **96**, 101115 1-3.
7 N. Gao, W. Lin, X. Chen, K. Huang, S. Li, J. Li, H. Chen, X. Yang, L. Ji, E. T. Yu and J. Kang, *Nanoscale*, 2014, **6**, 14733-14739.
8 F. Qian, Y. LI, S. Gradecak, H.-G. Park, Y. Dong, Y. Ding, Z. L. Wang and C. M. Lieber, *Nature mater.*, 2008, **7**, 701-706.

9 S. Nagahama, N. Iwasa, T. Yamada, T. Matsushita and Y. Sugimoto, *Jpn. J. Appl. Phys.*, 1996, **35**, L74-L76.
10 S. Nakamura, M. Senoh, N. Iwasa and S.-i. Nagahama, *Appl. Phys. Lett.*, 1995, **67**, 1868-1870.
11 T. C. Harman, P. J. Taylor, M. P. Walsh and B. E. LaForge, *Science*, 2002, **297**, 2229-2232.
12 R. Jin, G. Chen, J. Pei, J. Sun and Q. Wang, *CrystEngComm*, 2012, **14**, 4461-4466.
13 R. Venkatasubramanian, E. Siivola, T. Colpitts and B. O'Quinn, *Nature*, 2001, **413**, 597-602.
14 E. I. Rogacheva, O. N. Nashchekina, A. V. Meriuts, S. G. Lyubchenko, M. S. Dresselhaus and G. Dresselhaus, *Appl. Phys. Lett.*, 2005, **86**, 063103 1-3.
15 M. S. Dresselhaus, G. Chen, M. Y. Tang, R. Yang, H. Lee, D. Wang, Z. Ren, J.-P. Fleurial and P. Gogna, *Adv. Mater.*, 2007, **19**, 1043-1053.
16 P. Pichanusakorn and P. Bandaru, *Mat. Sci. Eng. R*, 2010, **67**, 19-63.
17 Y. Mune, H. Ohta, K. Koumoto, T. Mizoguchi and Y. Ikuhara, *Appl. Phys. Lett.*, 2007, 91, 192105 1-3.
18 S. Y. Ren and J. D. Dow, *Phys. Rev. B*, 1982, **25**, 3750-3755.
19 G. Chen, *Phys. Rev. B*, 1998, **57**, 958-973.
20 H. Ohta, S. Kim, Y. Mune, T. Mizoguchi, K. Nomura, S. Ohta, T. Nomura, Y. Nakanishi, Y. Ikuhara, M. Hirano, H. Hosono and K. Koumoto, *Nat. Mater.*, 2007, **6**, 129-134.
21 F. Li, J.-F. Li, L.-D. Zhao, K. Xiang, Y. Liu, B.-P. Zhang, Y.-H. Lin, C.-W. Nan and H.-M. Zhu, *Energ. Environ. Sci.*, 2012, **5**, 7188-7195.
22 J. W. Park, P. S. Jeong, S.-H. Choi, H. Lee, B. H. Kong and H. K. Cho, *Jpn. J. Appl. Phys.*, 2009, **48**, 111603 1-8.
23 I. Keller, W. Assenmacher, G. Schnakenburg and W. Z. Mader, *Anorg. Allg. Chem.*, 2009, **635**, 2065-2071.
24 D. K. Seo, B. H. Kong and H. K. Cho, *Cryst. Growth Des.*, 2010, **10**, 4638-4641.
25 J. H. Kim, D. K. Seo, C. H. Ahn, S. W. Shin, H. H. Cho and H. K. Cho, *J. Mater. Chem.*, 2012, **22**, 17595-17600.
26 A. I. Abutaha, S. R. S. Kumar and H. N. Alshareef, *Appl. Phys. Lett.*, 2013, **102**, 053507 1-3.
27 Y. Zhao, B. Chen, A. Miner and S. Priya, *RSC Adv.*, 2014, **4**, 18370-18377.
28 W. Xu, Y. Liu, B. Chen, D.-B. Liu, Y.-H. Linc and A. Marcellide, *Phys. Chem. Chem. Phys.*, 2013, **15**, 16312-16317.
29 K. Nomura, H. Ohta, K. Ueda, T. Kamiya and M. Orita, *J. Appl. Phys.*, 2004, **95**, 5532-5539.
30 L. L. Wu, F. W. Liu, Z. Q. Chu, Y. Liang, H. Y. Xu, H. Q. Lu, X. T. Zhang, Q. Li and S. K. Hark, *CrystEngComm*, 2010, **12**, 2047-2050.
31 Y. Kang, S. Lee, H. Sim, C. H. Sohn, W. G. Park, S. J. Song, U. K. Kim, C. S. Hwang, S. Han and D.-Y. Cho, *J. Mater. Chem. C*, 2014, **2**, 9196-9204.
32 G. H. Kim, H. S. Shin, B. D. Ahn, K. H. Kim, W. J. Park and H. J. Kim, *J. Electrochem. Soc.*, 2009, **156**, H7-H9.
33 S. Park, K.-H. Kim, J.-W. Jo, S. Sung, K.-T. Kim, W.-J. Lee, J. Kim, H. J. Kim, G.-R. Yi, Y.-H. Kim, M.-H. Yoon and S. K. Park, *Adv. Funct. Mater.*, 2015, **25**, 2807-2815.
34 J. Livage and C. J. Sanchez, *Non-Cryst. Solids*, 1992, **145**, 11-19.
35 K. Noboru, M. Isobe and M. Nakamura, *J. Solid State Chem.*, 1995, **116**, 170-178.
36 J. Alvarez-Quintana, E. Martínez, E. Pérez-Tijerina, S. A. Pérez-García, and J. Rodríguez-Viejo, *J. Appl. Phys.*, 2010, **107**, 063713 1-4.
37 T. Tsubota, M. Ohtaki, K. Eguchi and H. Arai, *J. Mater. Chem.*, 1997, **7**, 85-90.
38 P. Jood, R. J. Mehta, Y. Zhang, G. Peleckis, X. Wang, R. W. Siegel, T. Borca-Tasciuc, S. X. Dou, and G. Ramanath, *Nano Lett.*, 2011, **11**, 4337-4342.
39 Y. Kinemuchi, H. Nakano, M. Mikami, K. Kobayashi, K. Watari, and Y. Hotta, *J. Appl. Phys.*, 2010, **108**, 053721 1-6.
40 T. Tani, S. Isobe, W.-S. Seo and K. Koumoto, *J. Mater. Chem.*, 2001, **11**, 2324-2328.
41 F. Vigué, P. Vennéguès, C. Deparis, S. Vézian, M. Laügt and J.-P. Faurie, *J. Appl. Phys.*, 2001, **90**, 5115-5119.
42 H. K. Cho, J. Y. Lee, K. S. Kim and G. M. Yang, *Appl. Phys. Lett.*, 2000, **77**, 247-249.
43 Y. Golan, X. H. Wu, J. S. Speck, R. P. Vaudo and V. M. Phanse, *Appl. Phys. Lett.*, 1998, **73**, 3090-3092.

Graphical abstract

1. Title : "Combinatorial approach to solution-processed $InGaO_3(ZnO)_m$ superlattice films: Growth mechanisms and their thermoelectric properties"

2. Authors : Sung Woon Cho, Myoungho Jeong, Jun Hyeon Kima, Yong Hun Kwon, Hyoungsub Kim, Jeong Yong Lee and Hyung Koun Cho*

The strong single-phase among $InGaO_3(ZnO)_m$ films with superlattice structures showed superior thermoelectric power factors. The detailed microstructural growth evolution of single- and double-phase $InGaO_3(ZnO)_m$ films were investigated using transmission electron microscopy.